Modulated Upper-Hybrid Waves Coincident with Lower-Hybrid Waves in the Cusp

C. Moser[1], J. LaBelle [1], R. Roglans[2], J.W. Bonnell[2], Iver H. Cairns[3], C. Feltman[4], C.A. Kletzing[4], S. Bounds[4], R.P. Sawyer[5,6], and S.A. Fuselier[6,5],

to be submitted to Journal Geophysical Research: Space Physics

[1]Department of Physics and Astronomy, Dartmouth College, Hanover, NH

[2]Space Science Laboratory, University of California, Berkeley, CA

[3]School of Physics, University of Sydney, Sydney, AU

[4]Department of Physics and Astronomy, University of Iowa, Iowa City, IA

[5]Department of Physics and Astronomy, University of Texas, San Antonio, TX

[6]Space Science and Engineering Department, Southwest Research Institute, San Antonio, TX

Key Points:

- Modulated upper-hybrid waves coincided with enhanced power near the local lower-hybrid frequency.
- The spacings of the banded upper-hybrid waves are correlated with the frequency of the peak spectral density near the lower-hybrid peaks.
- Kinematic constraints and energy densities of wave modes suggest wave-wave process is plausible, with decay more likely than coalescence.

Abstract

During the Twin Rockets to Investigate Cusp Electrodynamics (TRICE-2) High-Flyer rocket's passage through the cusp the high frequency (HF) radio wave receiver observed three intervals of banded Upper-Hybrid (UH) waves. The bands begin at the UH frequency (∼1.2–1.3 MHz), descending to as low as 1.1 MHz, with amplitudes of hundreds of mV/m. The spacing of the bands are ∼4.5–6 kHz and the number of bands ranges from three to ten. Simultaneously, the very low frequency (VLF) radio wave receiver observed Lower-Hybrid (LH) waves with amplitudes ranging from 1–10 mV/m and frequencies of 4.5-6 kHz. Slight variations of the spacings of the bands in the UH waves were closely correlated with variations in the LH peak frequencies. Two possible wave-wave interactions are explored to explain this phenomenon: decay of an UH wave into a lower frequency UH wave and a LH wave, and coalescence of independent UH waves and LH waves that spawn UH waves. Using a dispersion relation calculator with electron and ion distribution functions based off those observed by the particle instruments suggests that UH waves, and to a lesser degree LH waves, can be excited by linear instabilities. Kinematic analysis of the waves dispersion relations and the wave matching conditions show that wave-wave interactions linking UH and LH modes are possible through either decay or coalescence. This analysis along with comparisons of the energy densities of the waves, and the ratio of their occupation numbers suggest that the decay process is more likely than coalescence.

1 Introduction

Many spacecraft missions have reported observations of Upper-Hybrid (UH) waves in the ionosphere, for instance as reviewed by LaBelle and Treumann [2002] and Benson [1993]. However, relatively few missions have observed detailed fine wave structures around the UH frequency in the ionosphere. Their high frequency, especially at low altitudes, requires a large bandwidth to measure with any detail. Benson [1993] showed the strongest UH emissions observed by the ISIS-2 satellite occurred under similar conditions required by the mechanism in Swift [1988], who suggested that UH waves are a significant source of heating for auroral electrons in the topside ionosphere. Colpitts and LaBelle [2008] observed Langmuir and UH waves with the SIERRA sounding rocket. Benson et al. [2004] observed UH waves with the IMAGE/RPI satellite and used these observations with the knowledge of the electron cyclotron frequency, f_{ce}, to determine the density of the plasma. The HIBAR mission was specifically designed to have a large bandwidth capable of measuring waves up to 5 MHz, and observed two intervals of UH waves in the ionosphere at approximately 377 and 390 km altitude [Samara et al., 2004]. These waves had electric fields of 2-20 mV/m and occurred just below the upper-hybrid frequency, $f_{UH} = 2f_{ce} = 2660$ kHz, with a banded-like structure of frequency spacings $4-8$ kHz and banded substructures with bands of $1-2$ kHz. This structure matches the prediction for UH wave eigenmodes. These modes appear when the UH waves are excited within a suitable scale of pre-existing density enhancements [Yoon et al., 2000]. The excitation process explains fine structure in auroral "roar" radio emissions observed at ground level [LaBelle et al., 1995; Shepherd et al., 1997].

Wave-wave interaction and modulated waves have been observed in plasma waves near the electron plasma frequency, f_{pe}, similar to those observed in this study at the UH frequency. Bonnell et al. [1997] performed a statistical study of several hundred Langmuir wave events from the FREJA satellite and SCIFER rocket which showed modulations occurring from 1-60 kHz. They also showed it was kinematically possible for decay of these waves with modulation > 7 kHz into oblique Langmuir and whistler waves. However, that study did not observed the lower-frequency waves thought to be associated with the modulations. However, Stasiewicz et al. [1996] presented studies of wave-wave interactions where the low frequency waves were observed, exploring two possible interpretations: decay of Langmuir waves into Lower-Hybrid (LH) waves, and coalescence of preexisting LH waves with the Langmuir waves, measurements confirmed by Lizunov et al. [2001] and Khotyainstev et al. [2001]. Cairns and Layden [2018] studied the theoretical decay of generalized Langmuir waves, which encompass the conventional Langmuir wave and UH wave, into backscattered Langmuir waves and ion acoustic or ion cyclotron waves for both weakly ($f_{ce} < f_{pe}$) and strongly ($f_{ce} > f_{pe}$) magnetized plasmas. For the latter case, the results show that as the wavevectors become more parallel to the background magnetic field the wave-number should increase, rather than decrease, for a three wave decay process.

Many experiments used ground based transmitters to inject powerful high-frequency waves into the ionosphere and observing the stimulated electron emissions (SEE). Leyser [1991] performed such an experiment wherein high-frequency waves were injected into the F-region. They excited UH waves and observed a downshifted maximum feature in the o-mode believed to come from the non-linear interaction of the UH waves with a LH wave that produced the EM wave. They used the Murtaza and Shukla [1984] two-fluid model of decay of an UH wave into an EM radio wave and a LH wave to explain their observations. They determining growth rates based on F-region plasma parameters at 200 km altitude. Leyser [1994] derived the non-linear dispersion relation for decay of UH waves into electromagnetic waves and LH waves for a collisionless, weakly magnetized plasma. They determined growth rates for frequencies near the LH frequency for various pump waves and F-region conditions. In a similar study, Gurevich et al. [1997] investigated the non-linear decay of an initial UH pump wave into a LH wave and a downshifted UH daughter wave in an inhomogeneous plasma when both the pump and daughter waves are trapped. They showed that leakage into Z-mode radiation plays an important role in the decay process and determined the critical field required for decay. Shvarts and Grach [1995] analyzed the dispersion relation for the decay of an UH wave into a lower frequency UH wave and an LH wave, and determined growth rates of waves near the LH frequency. These studies all considered overdense plasma conditions, $f_{pe}^2 >> f_{ce}^2$, which is not the case for our experiment, because our observations were at much higher altitudes.

This study presents observations from the Twin Rockets to Investigate Cusp Electrodynamics (TRICE-2) mission of banded structures in high frequency waves near the UH frequency at $f_{UH} \approx 1.2$ MHz coincident with low-frequency waves near the LH frequency at $f_{LH} \approx 5$ kHz. Section 2 describes the instruments and presents the observations showing these phenomena. Section 3 analyzes the stability of normal modes using WHAMP, a wave dispersion solver originally developed by Rönnmark [1982]. Section 4 derives the wave constraints through the kinematic equations for a three wave process. Section 5 and 6 discuss wave decay and coalescence as possible explanations and summarize the results, respectively.

2 Data Presentation

The TRICE-2 (Kletzing 52.003/004) mission consisted of two nearly identically instrumented sounding rockets, denoted High-Flyer and Low-Flyer, launched on 8 December 2018 at 08:26 and 08:28 UTC from Andoya Space Center, Norway, into active cusp aurora, with apogees of 1042 km and 756 km, respectively. The interplanetary magnetic field prior to launch had a steady negative B_z component of $\sim$5 nT, with ground optical and radar data confirming that ionospheric signatures of reconnection, such as polewardmoving auroral forms, were present during and following the launches (Kletzing et al., 2019). Both payloads encountered particle fluxes precipitating down the magnetic field lines, enhanced electron densities, and increases in the occurrence and intensity of plasma waves seen by the VLF and HF receiver, indicating traversal of an active polar cusp.

Dartmouth College provided a double probe antennas (6 cm dia., 30 cm center-center) mounted in the forward sections of the rockets, parallel to the spin axis and hence approximately parallel to the magnetic field, $\vec{B}$, since an attitude control system maintained the spin axis within 10° of $\vec{B}$. Associated HF receivers measured the resulting electric field component waveforms at frequencies of 100–5000 kHz, the upper bound determined by the 10-MHz sampling frequency and the lower bound determined by a high-pass filter designed to avoid having strong VLF waves saturate the receiver. The HF receiver included an automatic gain control (AGC) to optimize use of the dynamic range of the analog telemetry link used to transmit the waveforms from rocket to ground station. The AGC gain was folded into the data in post analysis using periodic calibration signals.

The University of California, Berkeley, provided 8 cm diameter probes E-field sensors mounted on the tips of 6.5-meter stacer booms oriented perpendicular to the rocket spin axes. Associated VLF receivers measured both resulting perpendicular electric field components over the frequency range 0–25 kHz. The DC electric field in the plane perpendicular to the magnetic field was also measured with this instrument, as well as the payload potential relative to the various probes. In addition, three-axis flux-gate magnetometers on each payload measured magnetic fields with $\pm 10\mu$T resolution over the frequency range 0-1.25 kHz.

Both The University of Iowa and Southwest Research Institute provided top-hat style electrostatic analyzers, the former measuring electrons (Energetic Electron Pitch Angle Analyzer–EEPAA) from 60–11486 eV with a time resolution of 50 ms and the latter ions (Ion Electrostatic Analyser–IESA) from 10eV–20keV with a time resolution of 384 ms. The University of Oslo provided Langmuir probes to measure the electron density with a 10kHz sample rate.

Figure 1a shows spectrograms of the HF (top panel) and VLF (middle panel) electric fields from the TRICE-2 High-Flyer, covering frequencies of 0–2 MHz and 0–25 kHz, respectively. The main part of the trajectory is included, starting at 08:29 (204 km), continuing through apogee at 08:36 UTC, and ending at 08:43 UTC (449 km). For this entire portion of the flight, the plasma frequency (f_{pe}) is less than the electron gyrofrequency (f_{ce}), which is around 1000 kHz. In this regime, the plasma frequency is evident as an upper cut-off of whistler mode auroral hiss; this cutoff can clearly be seen decreasing from ∼1000 kHz at 08:29 UTC to ∼ 250 kHz at 08:34 UTC as the rocket increased in altitude from ∼204-987 km, encountering decreasing electron density in the topside. The cutoff is again observed at the end of the interval increasing from 350 kHz and 08:40 UTC to 750 kHz and 08:43 UTC, as the rocket decreased in altitude from 857-449 km and encountered increasing electron density. In between, from 08:34:30-08:39:30 UTC, this pattern is interrupted by an increase in f_{pe} along with the intensity of the plasma waves themselves; during this interval the rocket traverses the polar cusp. In this region, UH waves also occur at frequencies exceeding f_{pe} and intense whistler waves occur below f_{pe}. (The apparent cutoff at approximately 100 kHz is due to the instrument's high pass filter as discussed above.) The VLF data (middle panel) also show a significant increase in the intensity of the waves in the cusp which persists poleward of the cusp. The VLF spectrum is dominated by whistler mode waves with lower frequency cutoff at the LH frequency $f_{LH} \sim 5$ kHz. Figure 1c (bottom panel) shows the differential energy flux of 60-2000 eV downgoing electrons from The University of Iowa EEPAA instrument. The cusp stands out as an interval of precipitating electrons up to 1000 eV from 08:34:30–08:39:00 UTC. The instrument detects low counts (∼10–20) of precipitating electrons before and after the rocket encounters the cusp.

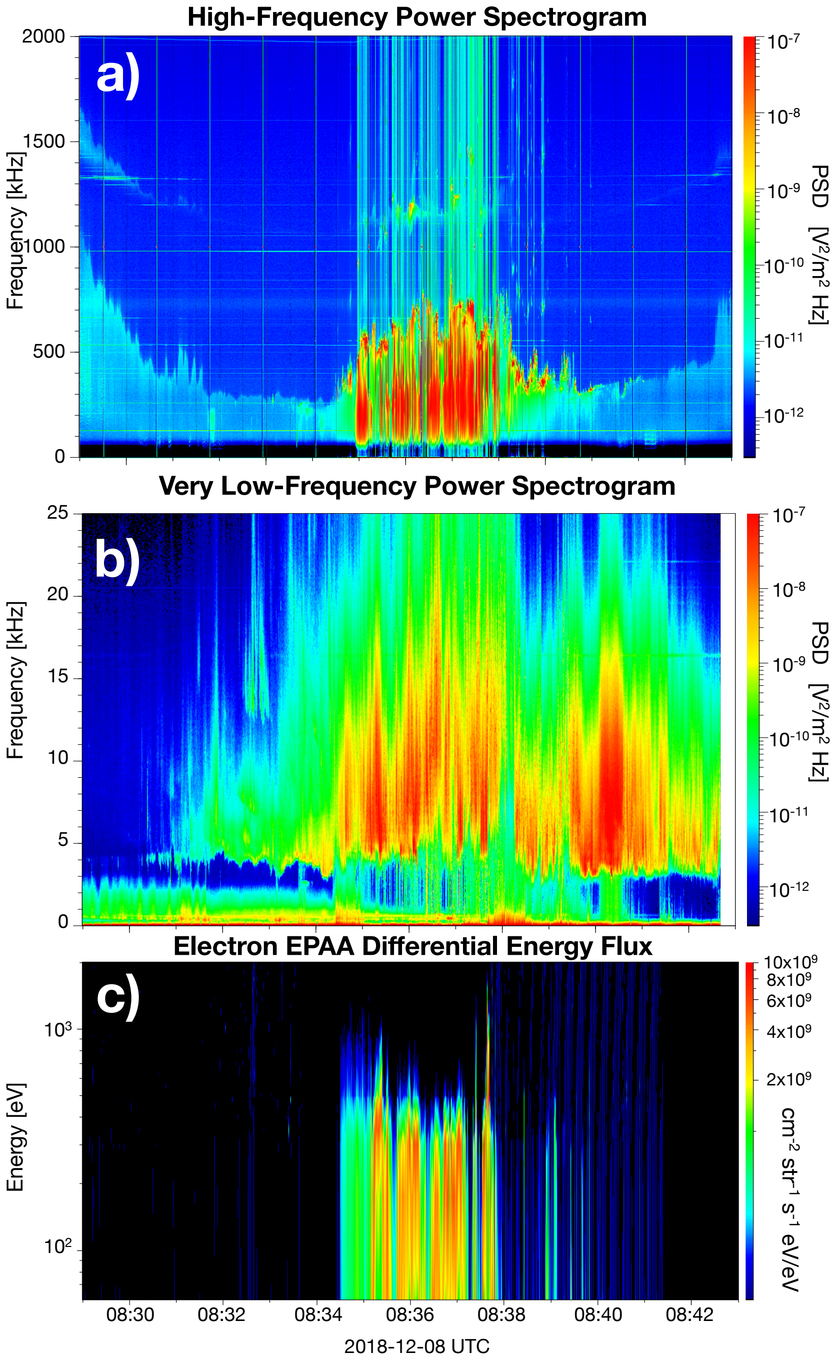

Figure 1: Spectrograms from 08:29-08:43 UTC during TRICE-2 High-Flyer's passage through the cusp. (a) HF wave power from 100–2000 kHz, showing an increase in the intensity and frequency of Langmuir waves between 08:34:30–08:39:30 UTC (frequencies 400–800 kHz) corresponding to the increase in density in the cusp. (b) VLF wave power from 0-25 kHz with intense broadband whistler waves occurring above the LH cutoff at ∼5 kHz within and poleward of the cusp. The Power Spectral Density (PSD) ranges from 10^{-13} to 10^{-6} for both the UH and LH spectrograms. (c) Differential Energy Flux of the electrons, increasing during the interval when the rocket is within the cusp.

Figure 2 shows expanded HF and VLF spectrograms that focus on two 25-second intervals when UH waves are observed. Figures 2a and 2c, covering 1080-1280 and 1150-1350 kHz, respectively, show details of the UH waves. The UH frequency, f_{UH}, calculated using the observed magnetic field and the plasma frequency implied by the Langmuir waves (wave cutoff in Figure 1) coincides with the upper boundary of these waves and is shown by a dashed white line in Figure 2. The distinctive feature of these waves is banded structures which intermittently occur and consist of up to 10 bands separated by approximately 5 kHz. For example from 08:35:49–08:35:51 UTC at 1170–1200 kHz there are roughly 6 distinct peaks at and below the UH frequency, and from 08:36:05–08:36:11 UTC from 1150–1240 kHz there are a varying number of distinct bands appearing at and below the UH frequency and again at 08:36:59–08:37:07 UTC from 1180–1300 kHz. Figures 2b and 2d, covering 0-25 kHz, show details of whistler mode and LH waves. Broadband whistler mode waves extending from near the LH frequency, f_{LH}, to above 25 kHz occur throughout these intervals. Separate from the broadband whistler mode waves are narrowband signals at $\sim$5 kHz, which may be interpreted as f_{LH}. In many cases, it is evident that the banded structure in the UH waves coincide with the distinctive narrow-band waves at the LH frequency, most notably starting at 08:36:04 UTC, but also near 08:35:50 UTC and 08:37:02 UTC.

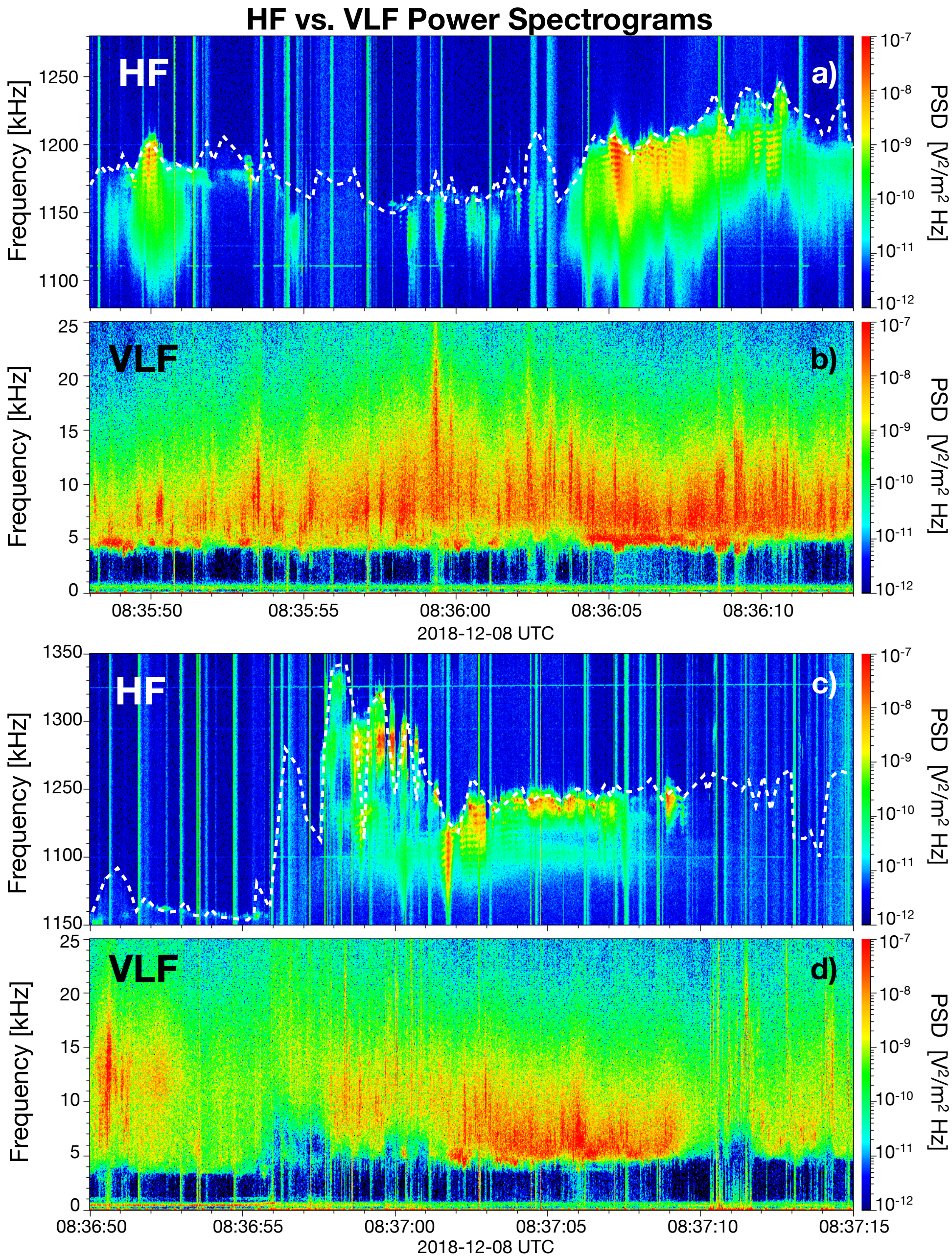

Figure 2: Expanded views of the HF and VLF spectrograms, showing the banded structure in the UH waves in the HF spectrograms and the distinct LH waves that occur below the broadband whistler mode waves in the VLF spectrograms at ∼5 kHz. The white line in panels (a) and (c) is f_{UH} calculated using the plasma frequency cutoff and the magnetometer data, at an altitude of ∼1000 km.

Figures 3a and 3e are even more greatly expanded HF and VLF spectrograms from 08:36:04.6-08:36:05.6 UTC (604.6-605.6 s post launch) at 1042 km altitude, one of the intervals identified above when banded UH waves coincide with narrowband waves at the lower hybrid frequency, intended for comparing the UH banding spacings with the LH wave frequencies. Figure 3a shows the HF spectrogram has up to 10 banded structures, while Figures 3b-d show individual spectra (slices through the spectrogram) at three selected times indicated by vertical lines in the spectrogram. The UH bands have rms amplitudes on the order of hundreds of mV/m. An automated method was developed to identify each of the spectral peaks, which are indicated by color coding in panels b-d. The position of each peak, and hence the frequency spacing between each pair of peaks, are calculated by finding the weighted centroid of each colored section of the spectrum. The mean value for all peak-to-peak differences detectable within each spectrum is given in the upper left corner of panels b-d. This mean band spacing significantly narrows across the three selected time intervals, from 5.18 ± 0.11 kHz at 604.8 s to 4.79 ± 0.13kHz at 605.18 s to 4.50 ± 0.09 kHz at 605.38 s.

Figure 3e shows the VLF spectrogram for the same time interval as Figure 3a, revealing the narrowband waves centered around the LH frequency, as well as broadband whistler mode waves extending above that frequency. The narrow band waves at f_{LH} exhibit slight variations in their peak frequency over time. Figure 3f-h show sets of three spectra for each of the three selected times as above, indicated by vertical lines in the spectrogram. The LH peak has rms amplitudes on the order of 1-10 mV/m. The same method used to identify the HF peaks was used to identify the centroids of the LH peaks. In panels f-h the main LH peak was identified as the distinctively strong signals starting at the lower bound where the spectra show a sharp cutoff and ending where the peaks drop off again before the broadband whistler waves begin. Peaks determined by this criterion are color coded in panels f-h. The frequency of the LH wave peak at each time interval was calculated as a weighted centroid for each of the colored spectra. The mean values of the three peaks measured in each panel are shown in the upper left corners of panels f-h. The frequency of maximum amplitude in the LH regime varies over each of the sub-intervals, and there are often several candidate peaks in the spectrum at any one time. This indicates a fairly non-stationary VLF spectrum, either from true temporal variation, spatial structure, or both, and complicates our interpretation of it relative to the spectral features in the UH regime. Even with this spectral variation, one can see that the mean frequency defined above decreases significantly from 5.08 ± 0.11 kHz at 604.8 s to 4.82 ± 0.11 kHz at 605.18 s to 4.56 ± 0.11 kHz at 605.38 s.

What is most striking about these observations is that the peak frequency of the LH waves not only closely matches the mean spacing of the UH bands (5.18 ± 0.11 versus 5.08 ± 0.11 kHz in the first, 4.79 ± 0.13 versus 4.82 ± 0.11 kHz in the second, and 4.50 ± 0.09 versus 4.56 ± 0.11 kHz in the third time interval), but these frequencies vary in the same manner as a function of time. This close correlation strongly suggests a connection between these waves.

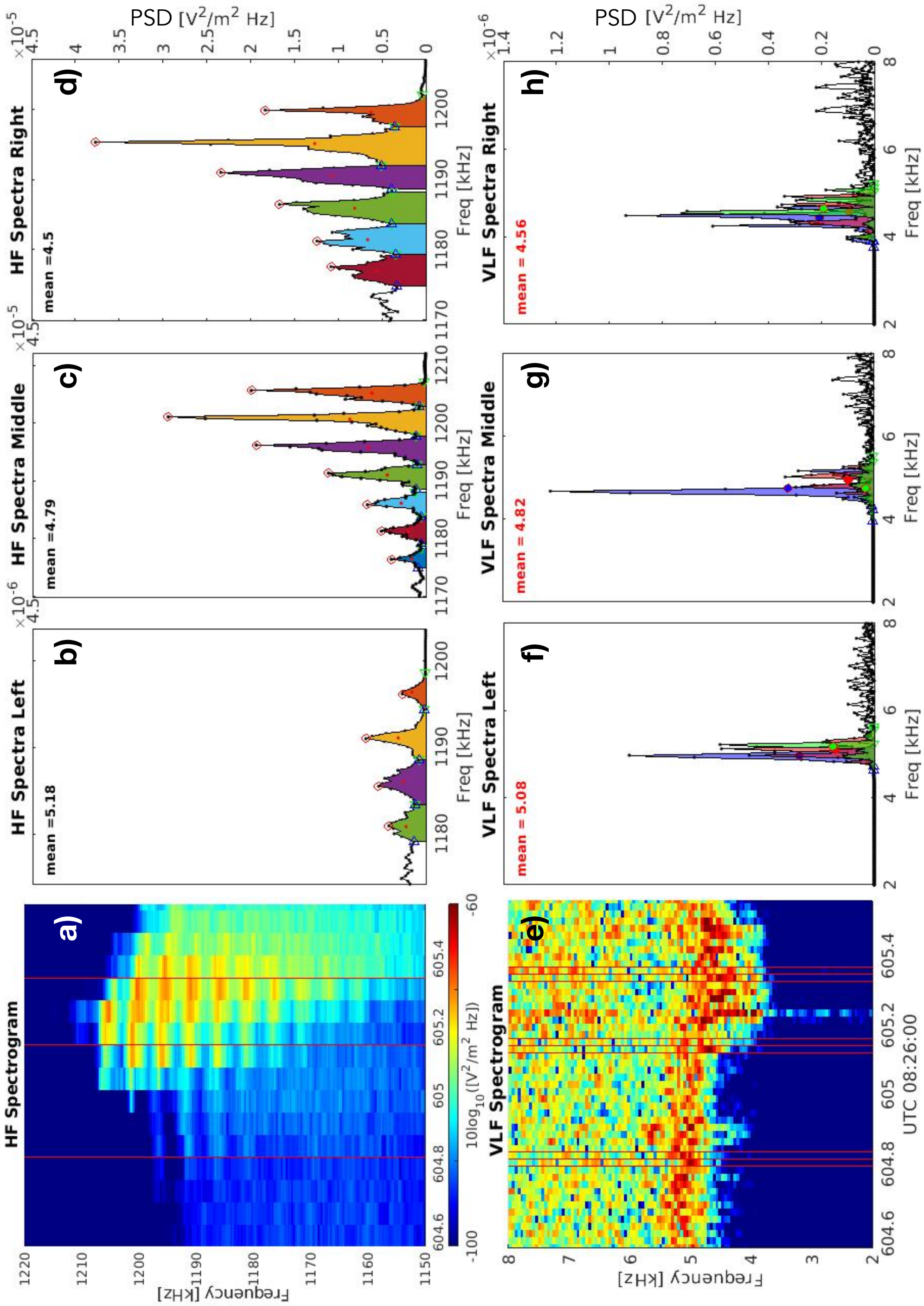

Figure 3: (a) Expanded HF spectrogram of banded structures for the time interval 08:36:04.6-08:36:05.6 UTC for frequencies 1150-1220 kHz. (e) Same time interval for the expanded VLF spectrogram from 2-8 kHz, showing peaks at f_{LH}. (b-d) Three selected spectra from the HF data showing the variation in peak spacings. (f-h) Nine selected spectra, three for each HF spectra, showing the peak variations over time. The HF spacing changes with the changes in frequency of the VLF peaks.

The analysis shown in Figure 3, comparing UH band spacings to LH wave peaks, was performed for 33 sets of HF and VLF spectra for which banded structures were identified in the former and had distinguishable LH wave peaks in the latter. The results are shown in Figure 4, where the average of the UH band spacing within each HF spectrum is plotted on the vertical axis against the average frequency of the corresponding three LH peaks plotted on the horizontal axis, with the standard deviations in each dimension (σ) indicated by bars. The linear correlation coefficient, an indicator of the strength of the linear relationship that has values between -1 and 1, is $r \approx 0.5$.

The data were fit to a straight line by finding the minimum χ^2 using equation (15.3.2) in Press et al. [1996] for linear fitting with errors in both coordinates with a confidence interval of 68.3% and an intercept value set to zero. Figure 4 shows the data with the fit results plotted as a black dashed lines with a slope of 1.02 ± 0.04 [kHz/kHz] and a reduced χ^2/ν of 0.89. The reduced χ^2/ν for the fit is an indicator of goodness-of-fit for the data, with values close to 1 indicating very good fits. A second linear fit was performed where the intercept was allowed to vary using equation (15.3.4) in Press et al. [1996] that resulted in a slope of 1.61 ± 1.25 [kHz/kHz] and an intercept of -2.94 ± 9.09 [kHz] with a reduced χ^2/ν of 0.53. The fit with zero intercept and a slope close to 1.0 is preferred based on physical grounds since it is consistent with the hypothesis that these banded structures in the UH waves are a result of wave-wave interaction with the LH waves. When the fit is allowed to vary both the slope and the intercept, the small frequency range of the data combined with uncertainties that are a significant fraction of the frequency range leads to large uncertainties in the fit that provide little information. However, the linear correlation coefficient, along with both slopes from the two fits, indicate a clear, positive correlation between the UH banding and the LH frequencies.

Because of the highly non-stationary aspect of the LH waves, and the multiple peaks in the spectra used in the averaging, it is possible the true modes that are correlated are not the largest amplitude peaks in all cases. Effect like this create uncertainties beyond the random uncertainties estimated as σ's in Figure 4 within the data used. Moreover, the ranges in the UH spacing and LH frequency are $\sim$10%–20%, very small for a reliable estimate of the gradient of the fitted line. In summary, the linear correlation coefficient and the linear fit show a clear correlation suggesting that the banding in the UH waves is due to a wave-wave interaction between the UH and LH waves.

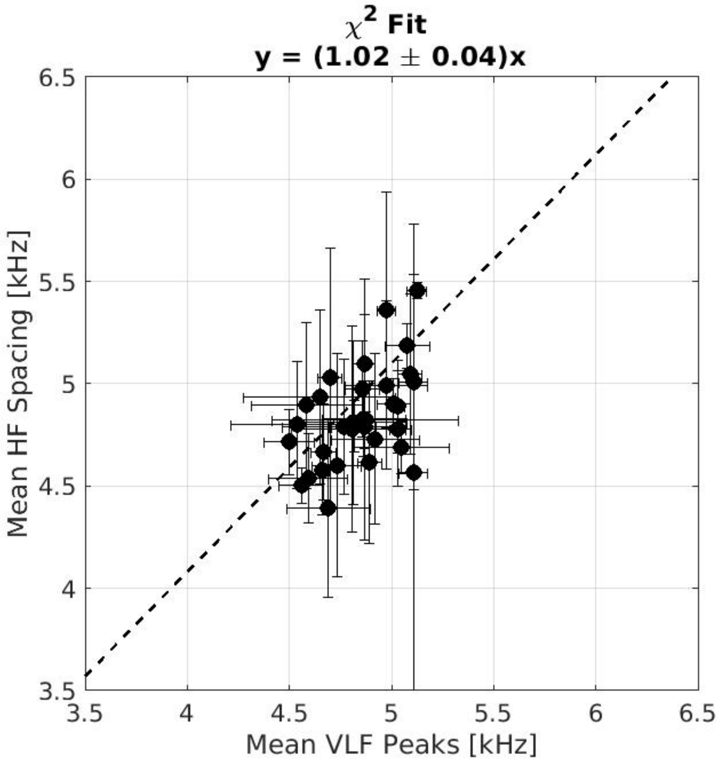

Figure 4: Plots of the average HF bands frequency spacings versus the average LH peak frequencies, with their respective standard deviations plotted as bars on the points. The linear fit (black dashed) is plotted and is based on the variances in both x and y, with a slope of 1.02 ± 0.04 [kHz/kHz].

3 Instability Analysis

To examine linear instabilities of upper hybrid and lower hybrid modes requires information about the electron distribution function for both modes, and the ion distribution function for the latter mode. There are two challenges here. First, even under the best circumstances, particle instruments on the TRICE2 High-Flyer rocket provide limited information about both distribution functions, limited by energy range and by angular, energy, and temporal resolutions. In the case of the ion distribution function the information is further limited because the ion detector did not fully deploy on the High-Flyer, affecting the measurements. Second, even if the spacecraft measurements cover the appropriate energy range with sufficient resolution, because temporal development of a strong instability rapidly reduces the unstable features of the distribution functions, it is rare to observe the fully unstable plasma; spacecraft instruments are believed to typically capture partially or even fully stabilized versions of the distributions.

With these limitations in mind, we developed a model electron distribution function based on data from the TRICE-2 High-Flyer EEPAA instrument. Figure 5a shows a selected measured distribution function from 08:36:03.894 UTC, which is during the second of three selected bursts of banded UH waves. This type of distribution is observed sporadically during the UH bursts, and is a rough guideline for the model distribution. Plotted is a cut through the distribution in the $v_{||}$–$v_{\perp}$ phase space for the velocity components parallel ($v_{||}$) and perpendicular ($v_{\perp}$) to the magnetic field $\vec{B}$; the 3D distribution would be obtained by revolving this plot around the $v_{||}$ axis. The instrument measures angles ranging from -10–190 degrees with respect to $\vec{B}$, and gyrotropy is assumed to fill out the distribution. This selected distribution is reminiscent of both a ring-beam and a losscone, peaked near 600 eV and with greater fluxes in the downgoing direction and, as expected, a dearth of flux in the upgoing direction. The peak phase space density is 5×10^{-14} m^{-3} (m/s)$^{-3}$ and integrating the distribution over the measured energy range yields a beam density of 60 cm^{-3} which is approximately 1% of the total density at this time ($n_{total} = 6080$ cm^{-3} inferred from the plasma frequency cutoff).

The WHAMP code (Rönnmark, 1982; Andres, 1985) used in this stability analysis requires the input distributions to be superpositions of drifting Maxwellians. Figures 5b and 5d show a model distribution composed of two distribution functions, each defined by $f(V_{||}, V_{\perp})$, a combination of drifting and non-drifting Maxwellians, in the form

$$
\begin{aligned}
f(V_{||}, V_{\perp}) &= \frac{n}{\pi^{3/2} u_{||}^3} e_1 (e_2 - e_3) \qquad (1)\\
e_1 &= e^{-(V_{||}/u_{||} - v_d)^2}\\
e_2 &= \frac{\alpha_1 - \alpha_2 \Delta}{\alpha_1(\alpha_1 - \alpha_2)} e^{-V_{\perp}^2/\alpha_1 u_{||}^2}\\
e_3 &= \frac{1 - \Delta}{\alpha_1 - \alpha_2} e^{-V_{\perp}^2/\alpha_2 u_{||}^2},
\end{aligned}
$$

where n is the beam density, $u_{||}$ the parallel thermal speed determined from the parallel temperature, T$_{||}$, α_1 the ratio of T$_{\perp}$/T$_{||}$ for the background distribution, α_2 the ratio of T$_{\perp}$/T$_{||}$ for the subtracted losscone, Δ the depth of the losscone (1 = no losscone, 0 = total losscone), and v_d the parallel drift velocity normalized to the parallel thermal speed. Table 1 gives the values of these parameters for the two distribution functions used to model the electron distribution shown in Figure 5a, which are called the losscone distribution and anisotropic Maxwellian, respectively, as well as the parameters assumed for the background cold electrons and ions. The cold background is assumed to have a temperature 2300 K, as is typical for the auroral ionosphere, and a density sufficient to make the total density equal to the value inferred from the plasma frequency cutoff. The ion composition is calculated using the equation for the LH frequency for multiple ion species:

$$\omega_{LH}^2 = \frac{\Omega_{ce}^2}{\omega_{UH}^2} \sum_{\sigma} \omega_{p\sigma}^2, \tag{2}$$

where ω_{LH} is the lower-hybrid frequency, ω_{ce} is the electron cyclotron frequency, ω_{UH} is the upper-hybrid frequency, and $\omega_{p\sigma}$ is the ion plasma frequency for each species. Fitting the data to equation (2) results in an ion composition of 7% hydrogen and 93% oxygen. This equation reduces to the approximation used in the kinematics derivation below (see equation (8)) for a single ion species.

Figure 5b shows the resulting model electron distribution, which resembles the measured distribution. The model ring distribution has a slightly larger beam density of 144 cm^{-3}, but a similar peak phase space density of 5×10^{-14} $\mathrm{m}^{-3}(\mathrm{m/s})^{-3}$. For reference, a horseshoe distribution was also developed to roughly match the measured electron distribution. The resulting growth rates were identical for the LH surface, and nearly identical for the UH surface.

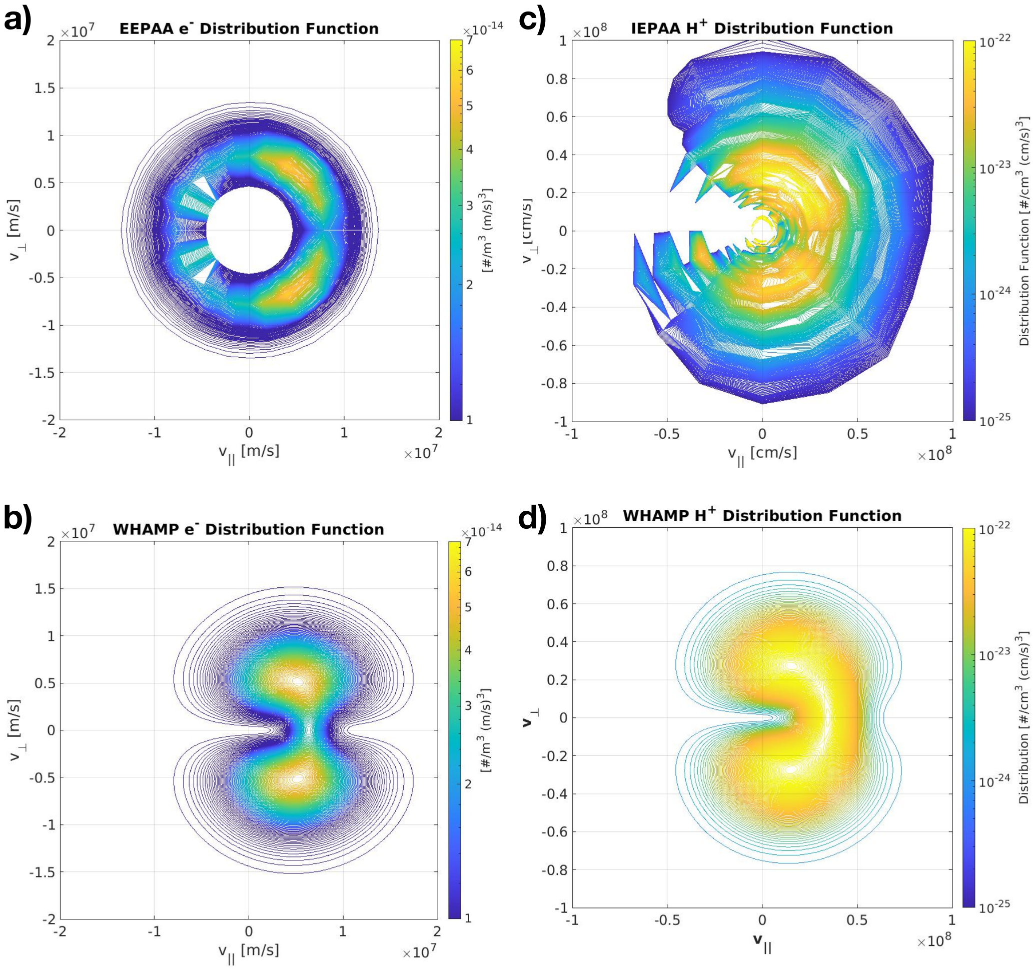

Figure 5: Electron and ion distributions measured during times of UH banding. (a) e^- distribution at 08:36:03.894 UTC and (c) is the H^+ distribution averaged over 08:35:49-08:37:06 UTC. Panels (b) and (d) are the corresponding model distributions defined by equation (1), with parameters given in Tables 1–2.

Full assessment of the growth rate of the LH waves requires the ion distribution function in addition to the electron distribution modeled above. For the ions, measurements provide even less guidance since the instrument did not deploy fully during flight, and therefore the data cannot give us a clear image of the distribution for the relevant time intervals. The ion instrument measured pitch angles from 0 to 360 degrees with respect to the background magnetic field. However, the partial deployment of the instrument resulted in reduced sensitivity, particularly in the upgoing direction (see Sawyer et al. 2021 for more details). Figure 5c shows the ion distribution measured by the ion

Table 1: Table of parameters used to generate a model of the observed EEPAA ring distribution, as well as the background electrons and ions species, used to generate the dispersion surfaces using WHAMP. The reference horseshoe distribution is listed in parentheses.

WHAMP Parameters	Losscone Distribution	Anisotropic Maxwellian	Background e^-	Background H^+	Background O^+
n_e [cm^{-3}]	140.0 (250)	4.0 (20)	5936.0	426.0	5654.0
$T_{\|\|}$ [eV]	100.0 (140)	12.0 (30)	0.2	0.2	0.2
α_1	0.7 (0.7)	3 (2)	1	1	1
α_2	1 (1)	0 (0)	0	0	0
Δ	0 (0)	1 (1)	1	1	1
$v_D/v_{\|\|}$	0.8 (0.5)	3.1 (2.2)	0	0	0

ESA averaged over the time interval 08:35:49-08:37:06 UTC where UH waves are observed. This figure roughly indicates a loss cone type distribution with energies in the range 150-1250 eV and peak phase space density of $8{\times}10^{-23}$ cm^{-3}(cm/s)$^{-3}$ and a density of 20 cm^{-3}. Figure 5d shows a model of this distribution function developed in the same manner as described above for electrons. Table 2 gives the parameters used in equation (1) to generate the ion distribution used in WHAMP.

Figure 6 shows the dispersion surfaces calculated with the WHAMP code (Rönnmark, 1982; Andres, 1985) for parameters given in Tables 1 and 2. Frequency on the vertical axis is normalized by the electron gyrofrequency, and wavevectors are normalized by the inverse electron gyroradius. Two surfaces are evident: the UH surface lies predominantly near $1.2f_{ce}$, with frequency decreasing in the high $k_\perp$ limit and at low $k_{||}$ where it becomes the Z-mode and is cutoff at the Z-cutoff near $0.4f_{ce}$. The whistler-LH surface lies at lower frequencies, approaching the lower hybrid frequency at high $k_\perp$ (and small $k_{||}$) and the plasma frequency at high $k_{||}$ (and small $k_\perp$). Red, orange, and yellow indicate regions where positive growth rate occurs exceeding an arbitrary threshold of 10^{-6} (normalized to f_{ce}) in the case of UH waves, and 10^{-8} in the case of LH waves. The LH modes

Table 2: Table of parameters used to generate a model of the observed ion ESA losscone distribution, as well as the background electrons and ions species, used to generate the dispersion surfaces using WHAMP.

WHAMP Parameters	Losscone Distribution	Anisotropic Maxwellian	Background e^-	Background H^+	Background O^+
n_e [cm^{-3}]	35.0	2.75	6080.0	388.25	5654
$T_{\|\|}$ [eV]	400.0	100.0	0.2	0.2	0.2
α_1	1.01	2	1	1	1
α_2	1	0	0	0	0
Δ	0	1	1	1	1
$v_D/v_{\|\|}$	0.5	2.5	0	0	0

can experience growth from the electron and ion distributions separately, represented by the yellow and orange regions, respectively. These growth rates are exceedingly low, but as mentioned above spacecraft instruments often do not resolve the unstable distribution because it is quickly reduced by production of the waves. Therefore this calculation is not intended to model the growth rate accurately for the actual electron and ion distributions present in the plasma, but instead indicates the frequency and wave-vector ranges for which wave growth occurs for the model distributions. The growth rate which generated the observed waves is presumably much larger than that inferred here from a model based on measured distributions. Electron distributions similar to that used to construct the model occurred sporadically during the UH wave bursts. Typical measured electron distributions in and around the cusp on TRICE-2 also had this ring-type form (see Figure 5a) but with somewhat lower energies. Models based on these lower energy distributions also yield unstable modes, but at higher $k_\perp$ values.

Upper hybrid wave growth occurs at frequencies within 20 kHz of the measured UH frequency, for modes strongly perpendicular to the magnetic field (top surface in Figure 6b). The values of $k_\perp$ range from 2.5 to 25 m^{-1}. The values of $k_{||}$ are an order of magnitude smaller. Predominantly perpendicular LH waves also exhibit growth, though much weaker than the UH waves for perpendicular wavenumbers of 0.25-10 m^{-1}.

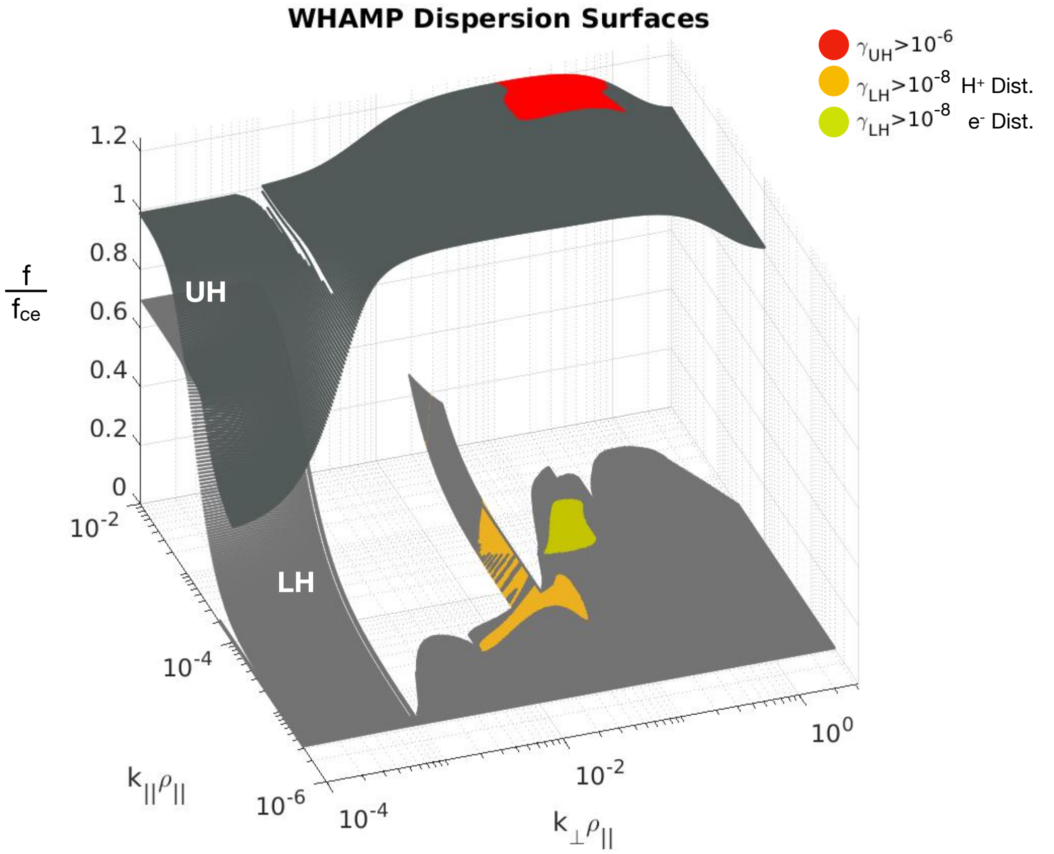

Figure 6: The UH and LH surfaces produced by WHAMP from the input distribution functions defined in Tables 1 and 2. The vertical axis is frequency normalized to the electron gyrofrequency, f_{ce}, and the perpendicular axes are the wavenumbers multiplied by the electron gyroradius. The highlighted red, orange and yellow regions are modes with growth rates, γ, greater than 10^{-6} for the UH and 10^{-8} for the LH, respectively, normalized to f_{ce}. The growth rates in the orange region are generated by the ion distribution, but the growth rates in the red and yellow regions are generated by the electron distribution.

4 Kinematics for Wave-Wave Interaction

The kinematics for a three wave non-linear process are determined now for both decay, where an initial UH wave decays into a LH wave and another UH wave ($UH \rightarrow$

UH'+LH), and coalescence, where independent UH and LH waves grow within the same volume and combine to form a second UH wave (UH+$LH \rightarrow UH'$). Written together as $UH \rightarrow UH' \pm LH$, these processes obey conservation of energy and momentum, where corresponding conservation conditions are

$$\omega_1 = \omega_2 \pm \omega_{LH} \tag{3}$$

$$\mathbf{k}_1 = \mathbf{k}_2 \pm \mathbf{k}_{LH} \ , \tag{4}$$

where $\mathbf{k}$ is the wavevector and ω the angular frequency. Assuming $k \approx k_\perp \gg k_{||}$, the dispersion relation for the UH waves is [Melrose, 1980]

$$\omega^2 = \omega_{UH}^2 + \frac{3k_{UH}^2 V_e^2 \omega_{pe}^2}{(w_{UH}^2 - 4\Omega_{ce}^2)} \tag{5}$$

$$\omega_{UH}^2 = \omega_{pe}^2 + \Omega_{ce}^2, \tag{6}$$

where the angular upper-hybrid frequency ω_{UH} is given by equation (6), ω_{pe} is the angular electron plasma frequency, V_e is the electron thermal speed, and Ω_{ce} is the angular electron cyclotron frequency. The dispersion relation for the LH waves is [Melrose, 1980]

$$\omega^2 = \omega_{LH}^2 \left(1 + \frac{m_i}{m_e} cos^2(\theta)\right) + \left(3 + \frac{3T_e}{4T_i}\right) k_{LH}^2 V_i^2 \tag{7}$$

$$\omega_{LH}^2 = \left((\Omega_{ce}\Omega_{ci})^{-1} + \omega_{pi}^{-2}\right)^{-1} \approx \Omega_{ce}\Omega_{ci}, \tag{8}$$

where the lower-hybrid frequency ω_{LH} is given by equation (8), m_i is the oxygen ion mass since the background ion composition is ~93% oxygen, m_e is the electron mass, V_i is the ion thermal speed, Ω_{ci} is the angular ion cyclotron frequency, θ is the angle between the LH wavevector and the background magnetic field, assumed to be nearly perpendicular, and $T_{i/e}$ are the ion/electron temperatures, assumed to be equal. The term $\alpha^2 = 1+\frac{m_i}{m_e} cos^2(\theta)$ is highly sensitive to the angle of propagation, with values between $9.9 \geq \alpha \geq 1$ for angles between 89^o-90^o. From these assumptions the LH dispersion relation becomes

$$\omega^2 \approx \alpha^2 \omega_{LH}^2 + 4k_{LH}^2 V_i^2. \tag{9}$$

Substituting the UH and LH dispersion relations (5) and (7), respectively, into (3) leads to

$$\omega_{UH}\left(1+\frac{3k_1^2V_e^2\omega_p^2}{\omega_{UH}^2\left(\omega_{UH}^2-4\Omega_{ce}^2\right)}\right)^{1/2}=\omega_{UH}\left(1+\frac{3k_2^2V_e^2\omega_p^2}{\omega_{UH}^2\left(\omega_{UH}^2-4\Omega_{ce}^2\right)}\right)^{1/2} \pm\alpha\omega_{LH}\left(1+\frac{4k_{LH}^2V_i^2}{\alpha^2\omega_{LH}^2}\right)^{1/2}, \qquad (10)$$

where the subscripts 1 and 2 denote the initial (UH) and second (UH') wave, respectively. Expanding the square root in the small argument limit for the first two terms leads to:

$$\omega_{UH}\left(1+\frac{3k_1^2V_e^2\omega_p^2}{2\omega_{UH}^2\left(\omega_{UH}^2-4\Omega_{ce}^2\right)}\right)=\omega_{UH}\left(1+\frac{3k_2^2V_e^2\omega_p^2}{2\omega_{UH}^2\left(\omega_{UH}^2-4\Omega_{ce}^2\right)}\right) \pm\alpha\omega_{LH}\left(1+\frac{4k_{LH}^2V_i^2}{\alpha^2\omega_{LH}^2}\right)^{1/2}. \qquad (11)$$

For the plasma environment presented here, $\omega_{LH} \ll \omega_{UH}$, and therefore the third term is much less than either of the first two, implying $k_1 \approx k_2$. For a more qualitative look at the wavevectors, equation (11) can be rearranged in the form

$$k_1^2 = k_2^2 \pm \frac{2\omega_{UH}}{3V_e^2\omega_p^2}\left(\alpha^2\omega_{LH}^2+4k_{LH}^2V_i^2\right)^{1/2}\left(\omega_{UH}^2-4\Omega_{ce}^2\right). \qquad (12)$$

For the given plasma parameters $\omega_{UH}^2 - 4\Omega_{ce}^2 < 0$, and for the decay process (+ sign), the wavevector $k_2 > k_1$. That is, the decay $UH \rightarrow UH' + LH$ must proceed from UH waves with smaller wavenumbers k_1 to UH waves with larger wavenumbers k_2 even as the wave frequency ω_1 exceeds ω_2 from equation (3). This is the definition of an inverse cascade. Since $k_1 < k_2$ but $\mathbf{k}_1 = \mathbf{k}_2 + \mathbf{k}_{LH}$ the LH wave must have a wavevector component anti-parallel to $\mathbf{k}_1$. For the coalescence process (- sign), the wavevector $k_2 < k_1$, which, leads to the LH wavevector having a component anti-parallel to $\mathbf{k}_1$. Figure 7 illustrates these two conditions.

A semi-qualitative analysis of the constraints on k_{LH} derived from the approximated LH dispersion equation (9) where we assume the LH waves are within 10% of the LH frequency, and $\alpha^2 = 1$, implies

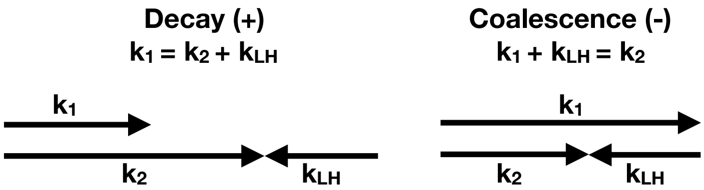

Figure 7: Diagrams of three wavevectors resulting from either decay or coalescence showing the relative size and direction of each wavevector.

$$k_{LH}^2 \approx \frac{|1.1 - 1|\omega_{LH}^2}{4V_i^2} \approx 10 \text{ m}^{-2} \tag{13}$$

For $\omega_{LH} \approx 2\pi \times 5$ kHz, and $V_i^2 = 2.4 \times 10^6 \text{m}^2/\text{s}^2$, ($k_B T_i = 0.2$ eV, oxygen ions predominate), this relation yields $\rho_{||} k_{LH} \approx 0.14$, where $\rho_{||}$ is the parallel electron gyroradius defined in WHAMP as $\rho_{||} = \sqrt{(2T_e/m_e)}/\Omega_{ce} \approx 0.04$ m. Similarly, a constraint on the UH wavevectors can be obtained using equation (4), assuming the UH wave is within 1% of the UH frequency,

$$k_1^2 = (0.99 - 1)\omega_{UH}^2 \frac{(\omega_{UH}^2 - 4\Omega_{ce}^2)}{3V_e^2\omega_p^2} \approx 14 \text{ m}^{-2} \tag{14}$$

where $V_e^2 = 7 \times 10^{10}$ m^2/s^2 ($k_B T_e = 0.2$ eV), $\omega_{LH} \approx 2\pi \times 5$ kHz, $\omega_{UH} \approx 2\pi \times 1220$ kHz, $\Omega_{ce} \approx 2\pi \times 1000$ kHz, $\omega_p \approx 2\pi \times 700$ kHz. This yields $\rho_{||} k_1 \approx 0.2$. Figure 7 shows the 2-D diagram of the decay and coalescence processes, showing the anti-parallel nature of the LH wavevector and primary UH wavevector $\mathbf{k_1}$, and how these wavevectors can be of the same order.

5 Decay versus Coalescence

These constraints on the wavevectors for the UH and LH waves ($\rho_{||} k_{LH} \propto 10^{-1}$ and $\rho_{||} k_1 \propto 10^{-1} \lessapprox \rho_{||} k_2$) are now compared to the dispersion surfaces. Figure 8 reproduces the dispersion surfaces generated by WHAMP; as in Figure 6 highlighted areas show ranges of **k**-space for which calculated growth rates exceed thresholds. Superposed on the plot are four sets of possible triplets of wave vectors that meet the criteria determined from kinematics (equations (3)–(4)). The wavevector for the initial UH wave, $\mathbf{k}_1$, is constrained to lie within the area of positive growth rate, and have a wave

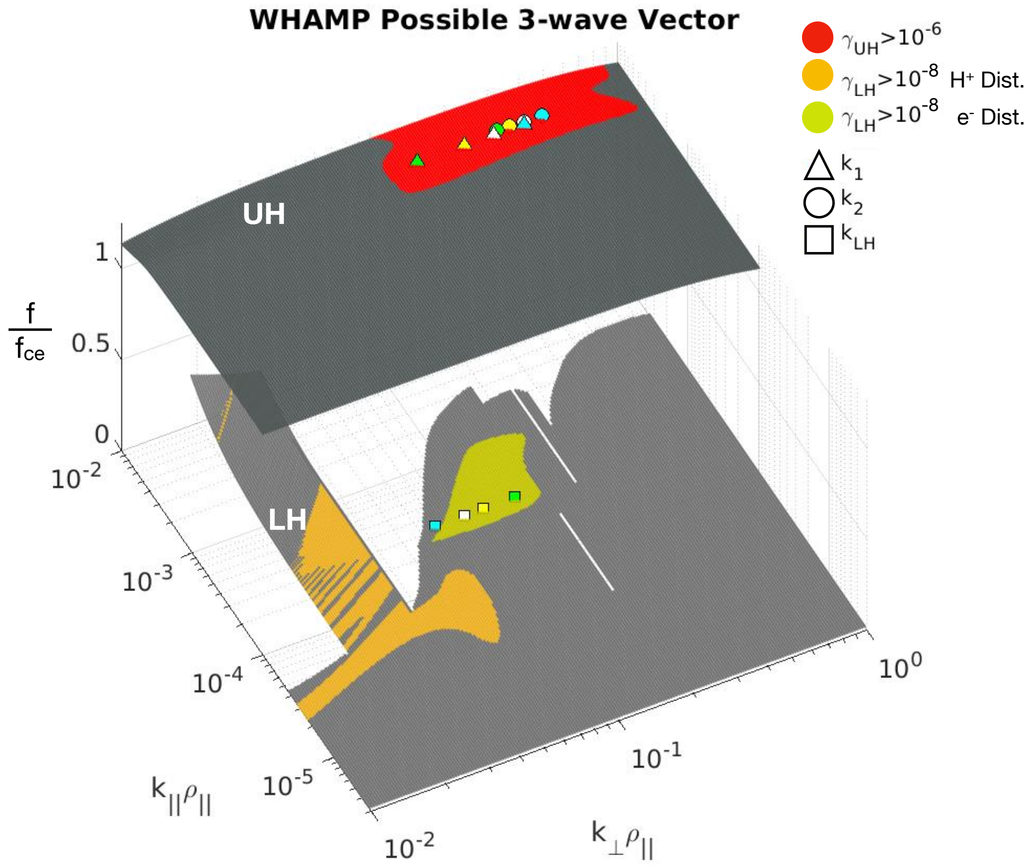

Figure 8: UH and LH dispersion surfaces focused on the areas of growth, where the plateaus roughly equal the UH and LH frequencies. On the UH surfaces, the four differently colored triangle points represent four possible initial UH wave-vectors. The four circles represent the corresponding second UH wave with a frequency difference of 5 kHz, matching in color. The LH surface shows the calculated LH wavevectors from equations (3)–(4) as squares matching in color.

frequency near the UH frequency. The wavevector for the secondary UH' wave, $\mathbf{k}_2$, must be close to the wavevector for the initial wave and correspond to a difference in frequency of ∼5 kHz from the initial UH frequency. For decay, $k_2 > k_1$ and $\omega_2 < \omega_1$, and for coalescence, $k_2 < k_1$ and $\omega_2 > \omega_1$. Both constraints are satisfied for the areas that exhibit growth on the UH surface in Figures 6 and 8, as the topology of the UH surface slopes down towards lower frequencies for higher wavenumbers.

The wavenumbers for the LH waves must fall on the portion of the surface in Figure 8 where their frequencies closely match the measured frequency; however, whether the wavevectors lie within areas of growth could support either decay or coalescence. If the LH waves lie within areas of growth, then the LH waves can be generated independent of the UH waves, and, if they occur within the same spatial volume as the UH waves, then the two waves could interact and spawn secondary UH waves with frequencies equal to the difference of the UH and LH wave frequencies. Of course, under these conditions, decay is also possible; in fact, growth or near growth conditions for the LH waves makes the decay process more efficient in producing the LH waves, since the LH wave-level us then non-thermal and this increases the nonlinear rate (see below). Otherwise, if this condition does not hold, then coalescence is unlikely and the waves would likely be generated by the decay of the initial UH wave. The WHAMP analysis using the particle distributions show that some of the chosen triplets of UH, UH' and LH waves all lie in areas of growth and some do not. This suggests that both decay and coalescence are possible.

Another analysis of the wave modes which may suggest which process is occurring involves examining the electric energy densities of the two waves and comparing them to the thermal energy density. An estimate of the electric energy densities $\epsilon_0 E_{rms}^2/2$ for the UH waves, using the average of the electric energy density for the 34 HF spectra used, is approximately 2×10^{-13} J/m^3. Similarly, the estimated electric energy density for the LH waves from the VLF spectra is $2{\times}10^{-16}$ J/m^3, 1000 times smaller than the UH waves. The thermal energy density of our system is estimated using nk_BT, where n is the density of the system ∼6080 cm^{-3}, and k_BT is the temperature of the background plasma, estimated to be ∼0.2 eV. This results in a thermal energy density on the order of 10^{-10} J/m^{-3}. The ratio of the electric to the thermal energy densities are on the order of 10^{-3} for the UH waves and 10^{-6} for the LH waves. These are consistent with the UH waves being driven to non-thermal, and probably non-linear levels, presumably by a linear instability. The same is true for the LH waves but less so because their ratio is smaller by a factor of 1000.

Comparing the different occupation numbers for the two waves gives a more quantitative understanding whether the LH waves are independent of the UH waves or a product of them. Melrose [1980] and others (e.g. Cairns [1987, 1988]) defined the relation between the occupation number and the measured wave electric fields by

$$\frac{1}{2}\epsilon_0 E^2 = \int \frac{d^3\mathbf{k}}{(2\pi)^3} R_i(\mathbf{k})\hbar\omega_i(\mathbf{k})N_i(\mathbf{k}) \tag{15}$$

where $R_i(\mathbf{k})$ is the ratio of electric to total energy in the mode i, $\omega_i(\mathbf{k})$ is the frequency of the mode, and $N_i(\mathbf{k})$ is the plasmon occupation number (related to the wave energy density at $\mathbf{k}$ for the modes i = UH, UH', and LH.) The WHAMP dispersion solver shows that the ratio of electric energy density to total energy density is approximately $R_i(\mathbf{k}) = 1/2$ for both the UH and LH waves. If we assume the angular distribution for the two sets of waves are symmetric with respect to the magnetic field, then the integral can be written

$$\mu_{Ei} = \frac{1}{2}\epsilon_0 E^2 = \int\int_{k_{min}}^{k_{max}} \frac{2\pi k_\perp dk_\perp dk_{||}}{(2\pi)^3}\frac{\hbar\omega_i(\mathbf{k})}{2}N_i(\mathbf{k}) \tag{16}$$

Since we know the frequencies for each wavevector from the dispersion surfaces, and they are roughly constant for the areas of interest, we can assume $\omega_{UH}(k) \approx 2\pi\times 1200$ kHz for the UH waves, and $\omega_{LH}(k) \approx 2\pi\times 5$ kHz for the LH waves. From this we can evaluate the ratio of the occupation numbers, assumed to be constant over the relevant wavevector domains, as

$$\frac{N_{UH}}{N_{LH}} = \frac{\mu_{E,uh}\omega_{lh}\left[\int\int k_\perp dk_\perp dk_{||}\right]_{lh}}{\mu_{E,lh}\omega_{uh}\left[\int\int k_\perp dk_\perp dk_{||}\right]_{uh}} = 4.17\times\frac{\left[\int\int k_\perp dk_\perp dk_{||}\right]_{lh}}{\left[\int\int k_\perp dk_\perp dk_{||}\right]_{uh}} \tag{17}$$

If we assume the integrals are over the same **k**-space volumes, which is reasonable since the values of the wavevectors of the two waves are similar (see equations (14) and (13)), the ratio is approximately 4 in equation (17) using the observed energy densities of UH and LH waves. However, the result is highly sensitive to the estimated ranges of wavevectors for each mode, which are poorly known. If the integrals are over different ranges of k-space for each wave, in particular if the LH wave occupies smaller wavevectors as suggested by where growth rates occur and our triplet wavevectors lie (see Figure 8), then the ratio of the occupation numbers may be less than 1.

By analogy with results for Langmuir waves and ion sound waves subject to decay and coalescence processes [e.g. Melrose 1980; Cairns 1987, 1988], the rate of change for the occupation number, $N_{UH'}$, for UH' waves in the decay and coalescence process obeys the approximate equations

$$\frac{dN_{UH'}}{dt} = \alpha - \Gamma_{UH'} N_{UH'} + \beta \left[N_{LH}(N_{UH} - N_{UH'}) \pm N_{UH} N_{UH'} \right]. \tag{18}$$

Here α is the rate for spontaneous emission, $\Gamma_{UH'}$ the linear damping rate of UH' waves, and β the appropriately averaged nonlinear rate coefficient.

Ignoring the spontaneous and linear terms, the nonlinear rate for UH' waves is always driven positively by the term $N_{UH} N_{LH}$. Accordingly, non-thermal levels of LH waves, corresponding to values of N_{LH} larger than the thermal level, will favor operation of both the decay and coalescence processes in (18), provided that $N_{UH} > N_{UH'}$. The final term in the brackets in (18) ($\pm N_{UH} N_{UH'}$) leads to exponential growth of UH' waves for the decay process (+) but exponential damping for the coalescence process (-). Ignoring the spontaneous emission and linear terms in equation (18), the decay should saturate ($dN_{UH'}/dt$ $= 0$) when

$$N_{LH}(N_{UH} - N_{UH'}) + N_{UH} N_{UH'} \simeq 0 \tag{19}$$

$$\text{or} \quad N_{UH} \simeq \frac{N_{LH} N_{UH'}}{N_{LH} + N_{UH'}} \tag{20}$$

Operation of the decay increases N_{LH} and $N_{UH'}$ by +1 for each UH plasmon lost from N_{UH}. Thus, if the decay proceeds towards saturation, i.e. N_{UH} proceeds from a large value towards a smaller value and $N_{UH'}$ and N_{LH} become much larger than their starting levels, then $N_{LH} \simeq N_{UH'}$ and equation (20) yields $N_{UH} \simeq N_{UH'}/2 \simeq N_{LH}/2$. Thus, semi-quantitatively, near saturation the decay has

$$N_{UH} \simeq N_{UH'} \simeq N_{LH}. \tag{21}$$

On the other hand, for the coalescence process saturation occurs when

$$N_{LH}(N_{UH} - N_{UH'}) - N_{UH}N_{UH'} \simeq 0 \quad (22)$$

$$\text{or} \quad N_{UH'} \simeq \frac{N_{LH}N_{UH}}{N_{LH} + N_{UH}}. \quad (23)$$

Even with N_{LH} and N_{UH} decreasing by +1 for each UH' plasmon produced, the primary constraint is that the process saturates when

$$N_{UH'} \simeq \min(N_{LH}, N_{UH}). \quad (24)$$

In this case the nonlinear process is unlikely to significantly affect the levels of LH and UH waves produced by their separate instabilities.

The results from equation (17), assuming the integrals are over similar **k**-space, show that $N_{UH} \simeq N_{LH}$ to within better than a factor of 10. The same is true for $N_{UH'} \simeq N_{LH}$, because the UH' energy densities are on the same order as the UH energy densities based on the observed wave levels in Figures 2 and 3. The simplest interpretation based on equations (21) and (24) is that the decay is active and is proceeding close to saturation. This explains semi-qualitatively the observed ratio of the UH and LH wave energy densities whether or not the wavenumbers are similar in magnitude or different in equation (17). This is also qualitatively consistent with multiple generations of decay proceeding to produce the multiple bands (> 2) of UH waves observed in Figures 2 and 3. An analogous situation is discussed by Cairns [1987, 1988] for 3$^{\text{rd}}$ and higher harmonics of f_{pe} radiation. If an interpretation involving coalescence is desired, then one must explain why the independent instabilities producing the UH and LH waves both independently result in very similar plasmon occupation numbers despite the results of equation (24) (e.g. $\min(N_{LH}, N_{UH}) \simeq N_{UH} \simeq N_{LH}$). This is a priori very unlikely. It is true, though, that if this situation occurs then multiple generations of the coalescence might occur.

6 Conclusion

The TRICE-2 High-Flyer HF wave receiver observed several intervals of modulated UH waves with frequency spacings of ∼5 kHz. Coincident with these waves are distinct peaks in the VLF power spectrogram near the LH frequency, at ∼5 kHz, below the broadband whistler mode waves. Analysis of the UH spacing variations compared to the LH peak location using a linear fitting model that took into account the errors in both sets of data showed a clear positive correlation between the two; furthermore, the best fit slope, for a fixed intercept of 0, was close to 1.0 as expected for wave-wave interaction. This result showed that these modes are likely interacting with one another. Using models of the electron and ion distribution functions based on measured distribution functions, a dispersion solver showed that the UH modes experience weak growth and the LH waves weaker or no growth. In both cases the growth rate may be underestimated. The kinematics of a three wave process for the UH and LH modes leads to estimates and constraints on the wave-numbers: $k_1 \gtrapprox k_2 > k_{LH}$ for coalescence, and $k_1 \lessapprox k_2 > k_{LH}$ for decay. These values were compared to the dispersion surfaces, and agreed with areas of growth. Another comparison was done between the ratio of the UH and LH energy densities to the thermal energy density, which are on the order of 10^{-3} and 10^{-6}, respectively. This comparison implies that waves are driven to non-linear levels by an instability, more so for the UH than LH. Comparing the occupation numbers of the modes, a more rigorous test of the process that is occurring, gives a result sensitive to the uncertain range of wavevectors for the different modes. However, if the **k**-range is similar for the two modes, which is implied by the areas of growth on the dispersion surfaces and the results from equations (13) and (14), then the occupation numbers are roughly equal. This suggests the decay process is observed and proceeding towards saturation. These results show that the observed modulated UH waves and peak LH waves seen in the power spectrum may plausibly result from a wave-wave interaction process.

Acknowledgments

Authors thank: David McGaw, Jeff Dolan, and Espen Trondsen for instrument engineering support; NASA, NSROC, and ASC personnel for supporting launch and payload functions. Research at Southwest Research Institute and The University of California, Berkeley was funded through the TRICE-2 mission grant NNX15AL08G. Research at Dartmouth and University of Iowa was supported by NASA grant NNX17AF92G.
Data from the TRICE-2 mission referenced within this article can be found at:
https://phi.physics.uiowa.edu/science/tau/data0/rocket/SCIENCE/TRICEII_Mission/

References

André, M. (1985). Dispersion surfaces. *Journal of Plasma Physics*, *33*(1), 1–19.

Beghin, C., Rauch, J., & Bosqued, J. (1989). Electrostatic plasma waves and hf auroral hiss generated at low altitude. *Journal of Geophysical Research: Space Physics*, *94*(A2), 1359–1378.

Benson, R., Webb, P., Green, J., Garcia, L., & Reinisch, B. (2004). Magnetospheric electron densities inferred from upper-hybrid band emissions. *Geophysical Research Letters*, *31*(20).

Benson, R. F. (1993). Elusive upper hybrid waves in the auroral topside ionosphere. *Washington DC American Geophysical Union Geophysical Monograph Series*, *80*, 267–274.

Bonnell, J., Kintner, P., Wahlund, J.-E., & Holtet, J. (1997). Modulated langmuir waves: observations from freja and scifer. *Journal of Geophysical Research: Space Physics*, *102*(A8), 17233–17240.

Cairns, I. H. (1987). Third and higher harmonic plasma emission due to raman scattering. *Journal of plasma physics*, *38*(2), 199–208.

Cairns, I. H. (1988). A theory for the radiation at the third to fifth harmonics of the plasma frequency upstream from the earth's bow shock. *Journal of Geophysical Research: Space Physics*, *93*(A2), 858–866.

Cairns, I. H., & Layden, A. (2018). Kinematics of electrostatic 3-wave decay of generalized langmuir waves in magnetized plasmas. *Physics of Plasmas*, *25*(8), 082309.

Colpitts, C., & LaBelle, J. (2008). Mode identification of whistler mode, z-mode, and langmuir/upper hybrid mode waves observed in an auroral sounding rocket experiment. *Journal of Geophysical Research: Space Physics*, *113*(A4).

Gurevich, A., Carlson, H., Lukyanov, A., & Zybin, K. (1997). Parametric decay of upper hybrid plasma waves trapped inside density irregularities in the ionosphere. *Physics Letters A*, *231*(1-2), 97–108.

Khotyaintsev, Y., Lizunov, G., & Stasiewicz, K. (2001). Langmuir wave structures registered by freja: analysis and modeling. *Advances in Space Research*, *28*(11), 1649–1654.

Kletzing, C., Fuselier, S. A., Bonnell, J. W., Labelle, J. W., Moen, J., Trattner, K. J., … Steven, P. M. (2019). The twin rockets to investigate cusp electrodynamics 2 (trice-2) mission. In *Agu fall meeting abstracts* (Vol. 2019, pp. SM34A–03).

LaBelle, J., & Treumann, R. A. (2002). Auroral radio emissions, 1. hisses, roars, and bursts. *Space Science Reviews*, *101*(3), 295–440.

LaBelle, J., Trimpi, M., Brittain, R., & Weatherwax, A. (1995). Fine structure of auroral roar emissions. *Journal of Geophysical Research: Space Physics*, *100*(A11), 21953–21959.

Leyser, T. (1991). Parametric interaction between upper hybrid and lower hybrid waves in heating experiments. *Geophysical Research Letters*, *18*(3), 408–411.

Leyser, T. (1994). Electromagnetic radiation by parametric decay of upper hybrid waves in ionospheric modification experiments. *Physics of Plasmas*, *1*(6), 2003–2011.

Lizunov, G., Khotyaintsev, Y., & Stasiewicz, K. (2001). Parametric decay to lower hybrid waves as a source of modulated langmuir waves in the topside ionosphere. *Journal of Geophysical Research: Space Physics*, *106*(A11), 24755–24763.

McAdams, K., Ergun, R., & LaBelle, J. (2000). Hf chirps: Eigenmode trapping in density depletions. *Geophysical Research Letters*, *27*(3), 321–324.

McAdams, K., & LaBelle, J. (1999). Narrowband structure in hf waves above the electron plasma frequency in the auroral ionosphere. *Geophysical Research Letters*, *26*(13), 1825–1828.

Melrose, D. (1980). Plasma astrophysics, vol. ii. *Gordon and Breach Science Publishers, New York (1979).*

Murtaza, G., & Shukla, P. (1984). Nonlinear generation of electromagnetic waves in a magnetoplasma. *Journal of Plasma Physics*, *31*(3), 423–436.

Press, W. H., Teukolsky, S. A., Vetterling, W. T., & Flannery, B. P. (1996). *Numerical recipes in fortran 90: Numerical recipes in fortran 77v. 2. numerical recipes in fortran 90.* Cambridge University Press.

Rönnmark, K. (1982). *Whamp-waves in homogeneous, anisotropic, multicomponent plasmas* (Tech. Rep.). Kiruna Geofysiska Inst.(Sweden).

Rönnmark, K. (1983). Computation of the dielectric tensor of a maxwellian plasma. *Plasma Physics*, *25*(6), 699.

Samara, M., LaBelle, J., Kletzing, C., & Bounds, S. (2004). Rocket observations of structured upper hybrid waves at fuh= 2fce. *Geophysical Research Letters*, *31*(22).

Sawyer, R., Fuselier, S., Kletzing, C., Bonnell, J., Roglans, R., Bounds, S., . . . George, D. (2021). Trice-2 observations of low-energy magnetospheric ions within the cusp. *Journal of Geophysical Research: Space Physics*, submitted.

Shepherd, S., LaBelle, J., & Trimpi, M. (1997). The polarization of auroral radio emissions. *Geophysical Research Letters*, *24*(24), 3161–3164.

Shvarts, M., & Grach, S. (1997). Interaction of upper and lower hybrid waves and generation of the downshifted maximum feature of stimulated electromagnetic emissions. *Journal of Atmospheric and Solar-Terrestrial Physics*, *59*(18), 2421–2429.

Stasiewicz, K., Holback, B., Krasnoselskikh, V., Boehm, M., Boström, R., & Kintner, P. (1996). Parametric instabilities of langmuir waves observed by freja. *Journal of Geophysical Research: Space Physics*, *101*(A10), 21515–21525.

Swift, D. W. (1988). A numerical model for auroral precipitation. *Journal of Geophysical Research: Space Physics*, *93*(A9), 9815–9830.

Yoon, P., Weatherwax, A., & LaBelle, J. (2000). Discrete electrostatic eigenmodes associated with ionospheric density structure: Generation of auroral roar fine frequency structure. *Journal of Geophysical Research: Space Physics*, *105*(A12), 27589–27596.